Quantification of the evaporation process during fragmentation of ^{12}C, ^{14}N, ^{16}O, and ^{20}Ne on elemental targets

Sukhendu De [1,*] V. Choudhary,[2,†] R. Chatterjee [1,‡] and W. Horiuchi [3,4,5,6,§]

[1]*Indian Institute of Technology Roorkee, Roorkee 247667, Uttarakhand, India*

[2]*Department of Physics, School of Science, JECRC University, Jaipur 303905, Rajasthan, India*

[3]*Department of Physics, Osaka Metropolitan University, Osaka 558-8585, Japan*

[4]*Nambu Yoichiro Institute of Theoretical and Experimental Physics (NITEP), Osaka Metropolitan University, Osaka 558-8585, Japan*

[5]*RIKEN Nishina Center, Wako 351-0198, Japan*

[6]*Department of Physics, Hokkaido University, Sapporo 060-0810, Japan*

(Received 15 March 2025; revised 12 May 2025; accepted 22 May 2025; published 6 June 2025)

This study examines charge-changing cross sections for ^{12}C, ^{14}N, ^{16}O, and ^{20}Ne projectiles on elemental targets (C, Al, Cu) at a beam energy of around 290 MeV/nucleon. The two-stage abrasion-ablation model is used, with the abrasion stage described via the Glauber model, incorporating validated single-nucleon density distributions from proton elastic scattering data. In the ablation stage, where particle evaporation occurs, the contribution to charge-changing cross sections is estimated using two approaches. First, a statistical decay model is employed to analyze the evaporation of protons following neutron removal in the abrasion stage. The second approach estimates evaporation contributions by subtracting the direct process component (abrasion) from the experimental charge-changing cross-section data. A comparison between these estimated contributions from the experimental data and the predictions of the statistical model enables a systematic evaluation of the evaporation process. The key factors influencing evaporation, such as excitation energy distribution parameters, decay width of the emitted particles, and nucleon separation energies, are analyzed. A strong correlation is observed between the maximum excitation energy available for evaporation and the neutron separation energy of the projectiles across different targets, highlighting the role of evaporation dynamics in the charge-changing cross sections.

DOI: 10.1103/PhysRevC.111.064604

I. INTRODUCTION: NUCLEAR FRAGMENTATION

The space radiation or galactic cosmic ray (GCR) environment is a complex mixture of photons, electrons, protons, and other heavy ions with energy ranging from a few eV to several TeV per nucleon. GCRs are emitted by sources beyond the solar system, principally supernovae, gamma-ray bursts, and other high-energy cosmic phenomena. As these intense particles move across space, they contact interstellar material and magnetic fields, which can trigger fragmentation and nuclear spallation [1], resulting in secondary particle creation. When high-energy heavy ions breach spacecraft shielding materials, they fracture into a slew of lesser ions with lower atomic numbers that can go deeper than the incoming particles. These nuclei in GCRs can have enough energy to pierce any shielding device currently employed on mission spacecraft. Interactions among the ions in the space environment are vital in various areas critical for space study and exploration due to the secondary radiation fields they generate. Space radiation may infiltrate housing, ships, equipment, and spacesuits, thereby putting personnel at risk. One of the most difficult issues in keeping astronauts fit and healthy while traveling through the solar system is minimizing the physiological changes produced by space radiation exposure [2]. Due to the difficulty of reproducing the GCR radiation environments on Earth, stochastic (Monte Carlo) or deterministic transport algorithms are required for risk assessment of exploratory mission scenarios and shielding design. Radiation transport algorithms employ fragmentation cross sections, also known as production cross sections, which include charge-changing cross sections, neutron removal cross sections, interaction cross sections, and total reaction cross sections to measure this phenomenon. The primary aim is to accurately model the interaction between particles and materials in space environments. The nuclear fragmentation cross sections used in space radiation transport codes at NASA are derived from experimental data and theoretical models. Experimental measurements [3–7] of nuclear fragmentation cross sections involve bombarding a target material with a beam of energetic particles and analyzing the resulting nuclear reactions. These experiments are typically performed using accelerators and detectors to measure the products of the interactions. Experimental data provide crucial information on the probabilities of various nuclear reactions and fragment production for different projectile energies and target materials. On the theoretical side, the required cross

*Contact author: sukhendu_d@ph.iitr.ac.in

†Contact author: vishal.choudhary@jecrcu.edu.in

‡Contact author: rchatterjee@ph.iitr.ac.in

§Contact author: whoriuchi@omu.ac.jp

sections are computed using some semiempirical models like the Silberberg-Tsao [8] model and a series of codes like NUCFRAG [9], NUCFRG2 [10], and NUCFRG3 [11] developed by NASA. There are also a few software packages that are used in cross-section estimation for space radiation applications, like GEANT4 [12], FLUKA [13], PHITS [14], and LISE++ [15].

A proper analysis of the fragmentation process and cross-section measurements are also useful ingredients for modeling the transport code for the use of ion beam therapy dose calculations and treatment planning. When charged particles travel through matter, they lose energy largely through interactions with the material's atomic electrons and nucleus. The depth of penetration of the particles affects the energy deposition. The Bragg curve describes the connection between particle energy deposition or stopping power and material penetration depth [16,17]. When the Bragg peak is considered, the interaction cross section or total reaction cross section directly affects the total energy deposition profile of the charged particles [18,19]. A higher cross-section value results in a wider and shallower Bragg peak. This is due to the fact that particles with bigger cross sections have more frequent contact, resulting in a more progressive loss of energy across a wider depth range. The values of the cross sections vary from ion to ion depending on the nuclear interactions the ion undergoes when traveling through the material or human body. The fragments or ions like ^{4}He and ^{12}C become very useful for radiation therapy because of their favorable depth to dose Bragg curve. Recent results [20,21] on ^{3}He and ^{12}O ions have also proven to be very useful in heavy ion beam therapy.

Nuclear fragmentation in heavy-ion collisions at intermediate energies has been a subject of extensive research over the past few decades [22–24]. Of particular interest are exotic nuclei, such as halo nuclei [22,25,26] with extended neutron distributions or bubble nuclei [27,28] with reduced central densities, which exhibit unique structural properties that influence reaction dynamics. These exotic features not only provide valuable insights into nuclear interactions but also play a critical role in understanding nucleosynthesis and the evolution of matter in astrophysical environments [29,30], such as supernovae and neutron star mergers.

The charge-changing cross sections across nuclei can be effectively described using the abrasion-ablation framework [31–34]. This process involves two principal mechanisms where proton removal plays a central role. In one scenario, abrasion of protons occurs during the initial impact, often accompanied by neutron removal, followed by neutron evaporation in the later stage. In the alternative scenario, neutrons are primarily removed during the initial phase, while subsequent evaporation leads to the loss of one or more protons along with additional neutrons. These distinct pathways collectively influence the final charge of the residual nucleus. In the abrasion step, nucleons from the overlapping zone of the projectile and target are abraded, depending on the impact parameter, resulting in the formation of excited remnants of the initial nuclei, known as prefragments. In the subsequent ablation step, these prefragments deexcite through the evaporation of light particles. The evaporation chain continues until the excitation energy of the prefragments falls below the particle emission threshold energies, resulting in the formation of the final fragments.

In this paper, we study charge-changing cross sections using the abrasion-ablation model for ^{12}C, ^{14}N, ^{16}O, and ^{20}Ne projectiles on elemental targets C, Al, and Cu at a beam energy around 290 MeV/nucleon. The abrasion stage, representing direct nucleon removal, is modeled using the Glauber formalism [35,36] with appropriate nuclear density distributions. The ablation stage is governed by statistical evaporation models [15] based on Hauser-Feshbach theory, which calculates the light particle evaporation probability from excited prefragments.

To assess the evaporation contributions, we compare statistical model calculations with estimates from experimental charge-changing cross-section data by subtracting the calculated abrasion component. The evaporation process depends on several key factors, including excitation energy distributions (EED), nuclear level densities, decay width ratios, and neutron/proton separation energies of the prefragment nuclei. A detailed analysis is performed to examine the influence of EED parameters across different targets, revealing a linear inverse correlation between the maximum excitation energy and the projectile neutron separation energy.

The paper is organized as follows. The theoretical formalism involving the abrasion-ablation formalism is briefly described in Sec. II, followed by the details of the results and discussions in Sec. III, and the summary and conclusions of the present work in Sec. IV.

II. THEORETICAL FORMALISM

A. Primary fragmentation or abrasion stage

The Glauber multiple scattering approach [35] is a credible theoretical model for calculating projectile fragmentation in high-energy collisions. Let a projectile of mass number A_P that consists of N_P neutrons and Z_P protons produce a fragment of mass number A_F with neutron number N_F and proton number Z_F in the collision with a target nucleus of mass number A_T. The differential cross section for the primary yield of the fragment with N_F neutrons and Z_F protons are written as the product of the density of states $\omega(E, Z_F, A_F)$ and an integral over impact parameter b [31,32,36],

$$\frac{d\sigma}{dE}(E, Z_F, A_F) = \omega(E, Z_F, A_F) \int d^2b\, [P_p(\mathbf{b})]^{Z_F} [P_n(\mathbf{b})]^{N_F} \times [1 - P_n(\mathbf{b})]^{N_P - N_F} [1 - P_p(\mathbf{b})]^{Z_P - Z_F}. \quad (1)$$

The integral represents the cross section for each primary fragment state as a sum over impact parameters, considering the probability that Z_F protons and $N_F = A_F - Z_F$ neutrons from the projectile do not scatter, while the remaining ones do. The terms $P_p(\mathbf{b})$ and $P_n(\mathbf{b})$ denote the probabilities that a proton or neutron from the projectile, respectively, does not collide with the target. $\omega(E, Z_F, A_F)$ is the density of states, which is calculated by counting all combinations of projectile holes consistent with the fragment's charge and neutron numbers [31]. Thus, the energy-integrated primary cross section $\sigma(E, Z_F, A_F)$ inherently includes the binomial

factor $\binom{Z_P}{Z_F}\binom{N_P}{N_F}$, a component that has been incorporated in several previous models [31,37]:

$$\sigma(E, Z_F, A_F) = \binom{N_P}{N_F}\binom{Z_P}{Z_F}\int d^2b\,[P_p(\mathbf{b})]^{Z_F}[P_n(\mathbf{b})]^{N_F} \times [1 - P_n(\mathbf{b})]^{N_P - N_F}[1 - P_p(\mathbf{b})]^{Z_P - Z_F}. \quad (2)$$

Now following the work in Ref. [38] we can calculate the required cross sections as follows.

The total reaction cross section is obtained by taking the sum of cross sections in all events where at least one nucleon is removed, which is given as

$$\sigma_R = \int d^2b[1 - [P_p(\mathbf{b})]^{Z_P}[P_n(\mathbf{b})]^{N_P}]. \quad (3)$$

The partial neutron removal cross section (σ_{-xn}) can be calculated from Eq. (2) by setting $Z_F = Z_P$. The cross section for removal of x neutrons from the projectile is

$$\sigma_{-xn} = \binom{N_P}{x}\int d^2b\,[P_p(\mathbf{b})]^{Z_P}[P_n(\mathbf{b})]^{N_P - x}[1 - P_n(\mathbf{b})]^{x}. \quad (4)$$

The total neutron removal cross section is calculated by adding all events with at least one neutron removed without disturbing the proton number in the projectile:

$$\sigma_{\Delta N} = \sum_{N_F=0}^{N_P-1}\sigma(N_F, Z_P) = \int d^2b[P_p(\mathbf{b})]^{Z_P}\{1 - [P_n(\mathbf{b})]^{N_P}\}. \quad (5)$$

The charge-changing cross section in the abrasion is measured by taking all the events in which at least one proton is removed and is written by subtracting the total neutron removal cross section from the total reaction cross section,

$$\sigma_{cc} = \sigma_R - \sigma_{\Delta N} = \int d^2b\{1 - [P_p(\mathbf{b})]^{Z_P}\}. \quad (6)$$

The probability $P_p(\mathbf{b})$ can be determined from the S-matrix concept using the optical potential. The eikonal S matrix is defined as $\mathcal{S}_p(\mathbf{b}) = \exp[i\chi_p(\mathbf{b})]$, for a projectile proton scattering from a target nucleus, where $\chi_p(\mathbf{b})$ is the eikonal phase shift function [36].

The eikonal phase shift function is calculated using the finite-range optical limit approximation (FROLA) within the framework of the Glauber model [35]. In this approach, the phase shift function is obtained by folding the nucleon densities of the projectile and target with a finite-range nucleon-nucleon profile function, thereby accounting for the spatial extension of the interaction between nucleons [39,40].

The phase shift function with the above description is given as

$$\chi_p(\mathbf{b}) = i\int d^2s\;\rho^P_{pz}(\mathbf{s})\int d^2t\,\big[Z_T\,\rho^T_{pz}(\mathbf{t})\Gamma_{pp}(\mathbf{b}+\mathbf{s}-\mathbf{t}) + N_T\,\rho^T_{nz}(\mathbf{t})\Gamma_{pn}(\mathbf{b}+\mathbf{s}-\mathbf{t})\big], \quad (7)$$

with the thickness function $\rho^{P(T)}_{Nz}$ related to the density by, e.g.,

$$\rho^{P(T)}_{Nz} = \int \rho^{P(T)}_{N}(\sqrt{\mathbf{s}^2 + z^2})dz, \quad N = p, n, \quad (8)$$

where z is the coordinate along the direction of the incident beam. The densities of the projectile (target) proton (neutron) are $\rho^{P(T)}_{p(n)}(r)$ and are normalized so that $\int \rho^{P(T)}_{p(n)}(r)d^3r = 1$. Then the S matrix

$$\mathcal{S}_p(\mathbf{b}) = \exp\Big(-\int d^2s\rho^P_{pz}(\mathbf{s})\int d^2t\big[Z_T\,\rho^T_{pz}(\mathbf{t})\Gamma_{pp}(\mathbf{b}+\mathbf{s}-\mathbf{t}) + N_T\,\rho^T_{nz}(\mathbf{t})\Gamma_{pn}(\mathbf{b}+\mathbf{s}-\mathbf{t})\big]\Big), \quad (9)$$

where $\mathbf{s}\,(\mathbf{t})$ represents the two-dimensional coordinate of a particular projectile (target) nucleon relative to the center of mass of the projectile (target) nucleus, which lies on the plane perpendicular to the incident momentum of the projectile. The profile function $\Gamma_{pN}(\mathbf{b})$ $(N = p, n)$ describes the scattering of projectile protons (neutrons) with the target protons (neutrons), which is often parametrized in a finite range [41] as

$$\Gamma_{pN}(\mathbf{b}) = \frac{1 - i\alpha_{pN}}{4\pi\beta_{pN}}\sigma^{\rm tot}_{pN}\exp\left(-\frac{\mathbf{b}^2}{2\beta_{pN}}\right). \quad (10)$$

The parameters used in the proton-nucleon (pN) scattering model are defined as follows: α_{pN} is the ratio of the real part to the imaginary part of the pN scattering amplitude in the forward direction, $\sigma^{\rm tot}_{pN}$ denotes the total pN cross section, and β_{pN} is the slope parameter of the pN differential cross section, characterizing the spatial distribution of the scattering amplitude. The proton-proton (Coulomb removed) and proton-neutron total cross-section ($\sigma^{\rm tot}_{pN}$) parameters are generally obtained from a fit of experimental data. The standard parameter set for proton-neutron and proton-proton scattering can be found in tabulated form in Ref. [41]. The probability in Eq. (1) is then calculated as $P_p(\mathbf{b}) = |\mathcal{S}_p(\mathbf{b})|^2$. Similarly, the probability $P_n(\mathbf{b}) = |\mathcal{S}_n(\mathbf{b})|^2$, given by interchanging the role of a proton with a neutron ($p \leftrightarrow n$) in Eqs. (9) and (10).

B. Secondary fragmentation or ablation stage

In the ablation stage [31–33,37,42], the final fragmentation products are formed by deexciting the residual fragment in the abrasion stage through the evaporation of light particles. Here, we are interested in the process where neutrons are removed during the initial abrasion stage, followed by the evaporation of protons during the final stage.

The proton particle evaporation contribution is calculated following the development by Refs. [33,34]:

$$\sigma^{\rm evap}_{cc} = \sum_{x=1}^{N_P}\sigma_{-xn}P_{-xn}, \quad (11)$$

with σ_{-xn} as the partial neutron removal cross section in the abrasion stage as formulated in Eq. (4). P_{-xn} is the corresponding charged-particle evaporation probability after initial neutron removal, that depends on the EED of the prefragment and the probability of evaporation of at least one proton at a certain excitation energy:

$$P_{-xn} = \int_0^\infty w_{-xn}(E_{\rm ex})f(E_{\rm ex}, A_P - x, Z_P)\,dE_{\rm ex}. \quad (12)$$

$E_{\rm ex}$ is the excitation energy of the residual fragment after x-neutron removal, $f(E_{\rm ex}, A_p - x, Z_p)$ is the proton evaporation probability (same as the branching ratio) at a certain excitation energy, and $w_{-xn}(E_{\rm ex})$ is the EED of the prefragment. The

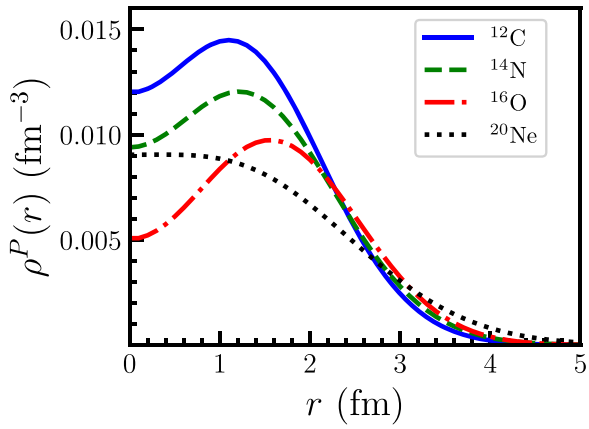

FIG. 1. Single-nucleon density distributions for ^{12}C [45], ^{14}N, ^{16}O [45], and ^{20}Ne [46]. For more details, see the text.

Gaimard-Schmidt (GS) approach [42] is used to calculate the EED of the residual fragment as in Refs. [33,34]. The LISE++ (GEMINI++) [43,44] code calculates the charged-particle evaporation probability $[f(E_{\rm ex}, A_P - x, Z_P)]$ at a certain excitation energy based on the Hauser-Feshbach theory and Weisskopf-Ewing formalism.

III. RESULTS AND DISCUSSIONS

In this section, we briefly present the results of charge-changing cross sections [Eq. (6)] calculated in the abrasion stage that uses the Glauber model with realistic density inputs. We then calculate proton evaporation contributions in the ablation stage and analyze their correlation with key influencing factors related to the evaporation process.

A. Single-nucleon density inputs

We now show a few input density configurations for ^{12}C, ^{14}N, ^{16}O, and ^{20}Ne in Fig. 1, considered in the literature. These different density configurations were examined in detail in Refs. [45–47] through comparison with elastic scattering and total reaction cross-section data, as well as electron scattering. Based on these studies, the most appropriate density configurations are a mixture of shell model and cluster configurations [48,49] type (M type) for ^{12}C, a 4α cluster type (C type) for ^{16}O, and a ^{16}O +α (O-α type) bicluster structure for ^{20}Ne. The density of ^{14}N is calculated using shell model configuration with a harmonic oscillator (HO) basis.

Our study will use these specific density distributions for cross-section calculations in the abrasion step, ensuring consistency with the most appropriate structure models. Nevertheless, had one considered an empirical type density for ^{12}C, ^{16}O, and ^{20}Ne, with parameters adjusted from elastic electron scattering data, the charge-changing cross sections would have been the same over a wide range of beam energies, as shown in the Supplemental Material [50] (see also Refs. [51–53] therein).

B. Direct fragmentation or abrasion stage

Table I presents the charge-changing cross section for projectile nuclei ^{12}C, ^{14}N, ^{16}O, and ^{20}Ne on elemental targets such as carbon (C), aluminum (Al), and copper (Cu) with beam energy 290 MeV/nucleon, during the direct fragmentation (abrasion) stage. The cross sections calculated using FROLA correspond to the most appropriate density configurations, as discussed in the previous section. These cross sections show slight variations when compared to other density configurations, with differences generally within 2%.

TABLE I. Charge-changing cross sections in the abrasion stage of projectile fragmentation for ^{12}C, ^{14}N, ^{16}O, and ^{20}Ne on elemental targets C, Al, and Cu at a beam energy of 290 MeV/nucleon. Calculations were performed using FROLA with the most appropriate nuclear density inputs: mixed-type (M type) density for ^{12}C, a shell model with a harmonic oscillator basis for ^{14}N, C type (4α cluster) density for ^{16}O, and a ^{16}O +α cluster configuration for ^{20}Ne. All cross sections in this table are rounded off to the nearest integer.

Projectile Nucleus	Target Nucleus	Projectile Density Type	$\sigma_{\rm cc}$ (mb) (Abrasion)
^{12}C	C	M type	650
	Al		1001
	Cu		1568
^{14}N	C	HO type	720
	Al		1070
	Cu		1648
^{16}O	C	C type	772
	Al		1130
	Cu		1722
^{20}Ne	C	O-α type	911
	Al		1308
	Cu		1951

Figure 2 shows the FROLA calculation for the charge-changing cross sections ($\sigma_{\rm cc}$) on the elemental targets, as a function of beam energy. The results in the abrasion stage ($\sigma_{\rm cc}$) systematically underestimate charge-changing cross sections compared to experimental data, as also observed in previous studies [34,54]. The charge-changing cross section represents the probability that an incident nucleus undergoes a change in charge, typically through the loss of one or more protons during its interaction with a target nucleus. In the FROLA implementation of the Glauber model, only the interactions of projectile protons with the target are considered, with the projectile neutrons being treated as spectators. This effectively models the direct removal of protons from the projectile. Since the charge-changing cross section is often considered a direct probe of the rms proton radius ($\tilde{r}_p$) of nuclei [39], the Glauber model requires modification to include the contribution of neutrons [55,56] in order to extract information on $\tilde{r}_p$ more accurately.

Different studies have adopted various possible methods to incorporate neutron contributions into the analysis. Some studies [54,57,58] propose using a phenomenological energy dependent or Z/N ratio dependent correction parameter that accounts for the contribution of neutrons in the projectile, allowing for a more precise description of the data. Despite the applied corrections, these models still fail to accurately describe the full energy range or the entire span of Z/N ratios of the projectiles. The authors of Ref. [60]

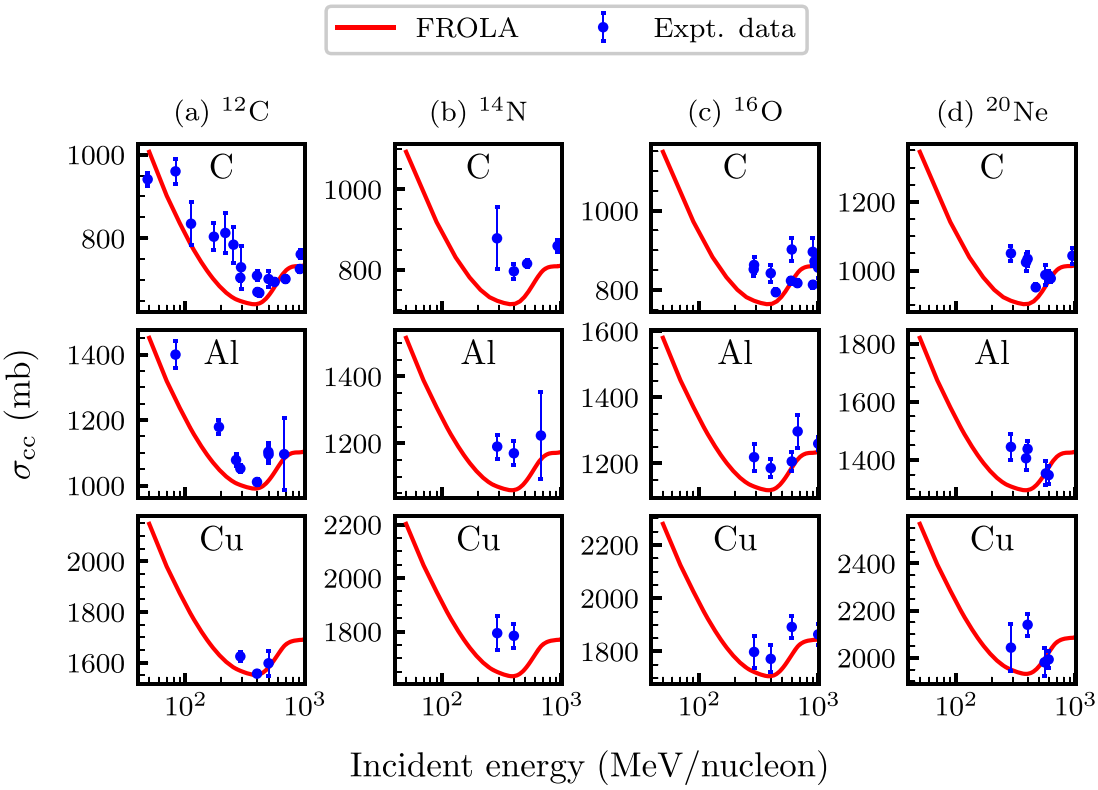

FIG. 2. Charge-changing cross section as a function of incident energy of the projectile nucleus for ^{12}C, ^{14}N, ^{16}O, and ^{20}Ne on elemental targets: Carbon (C), aluminum (Al), and copper (Cu). The plots are organized into four columns corresponding to different projectiles: (a) ^{12}C, (b) ^{14}N, (c) ^{16}O, and (d) ^{20}Ne. Each column presents the results for the respective projectiles on three targets: Carbon (C), aluminum (Al), and copper (Cu). The solid line represents theoretical calculations using the FROLA, and experimental data for the charge-changing cross sections in the energy range from 40 to 1000 MeV/nucleon are included, which are taken from Refs. [5,59–66] for ^{12}C, from Refs. [5,61,63,66] for ^{14}N, from Refs. [5,54,61–63,66] for ^{16}O, and from Refs. [5,66–68] for ^{20}Ne.

attempted to reproduce σ_{cc} for $^{12}C + ^{12}C$ by tuning the slope parameter β_{pN}, but their model underestimated the data at 200–400 MeV/nucleon.

A potential way to account for the contributions of neutrons to the charge-changing cross section is to incorporate the effects of proton evaporation from intermediate prefragments after initial direct neutron removal alongside direct proton removal in the Glauber model. In a sense, if one considers projectile fragmentation as a two-step process, i.e., direct removal followed by evaporation (abrasion plus ablation), then the Glauber model provides the best estimate for the direct proton removal contribution. This is why the Glauber model is important, and we used it to calculate the initial step (abrasion) in the charge-changing cross sections.

In reality, charged particles, predominantly protons, can be emitted following the direct removal of neutrons, especially when the prefragment is in a highly excited state [33,34,69]. When neutrons are removed from the projectile during the abrasion stage (direct fragmentation), the residual nucleus may become excited to states beyond the particle evaporation threshold. In such cases, deexcitation occurs through the removal of charged particles, such as protons or alpha particles. This process contributes to the overall charge-changing cross section, increasing the likelihood of charge-changing reactions beyond the initial neutron removal. This motivates us to explore the proton evaporation contribution to the charge-changing process on various elemental targets (C, Al, Cu) in the next section.

C. Proton evaporation contributions

Estimating proton evaporation contributions in the secondary fragmentation or ablation stage is done in two ways. The first involves evaporation contributions calculated following Eqs. (11) and (12). The second is subtracting the direct process (estimated with the FROLA) from the experimental data. A comparison of these two methods would then be made at the end.

Equation (11) involves calculations of partial neutron removal cross section (σ_{-xn}) and proton evaporation probability (P_{-xn}). The probability, in turn, depends on key factors like EED of the prefragment and probability at a particular excitation energy. We now proceed to present the calculations of these factors in detail.

1. Excitation energy distribution (EED)

The EED $w_{-xn}(E_{ex})$ of the prefragment, which is an important parameter in Eq. (12), is calculated using the LISE++ simulation code [15]. LISE++ offers several theoretical approaches for determining the EED, with the Gaimard-Schmidt

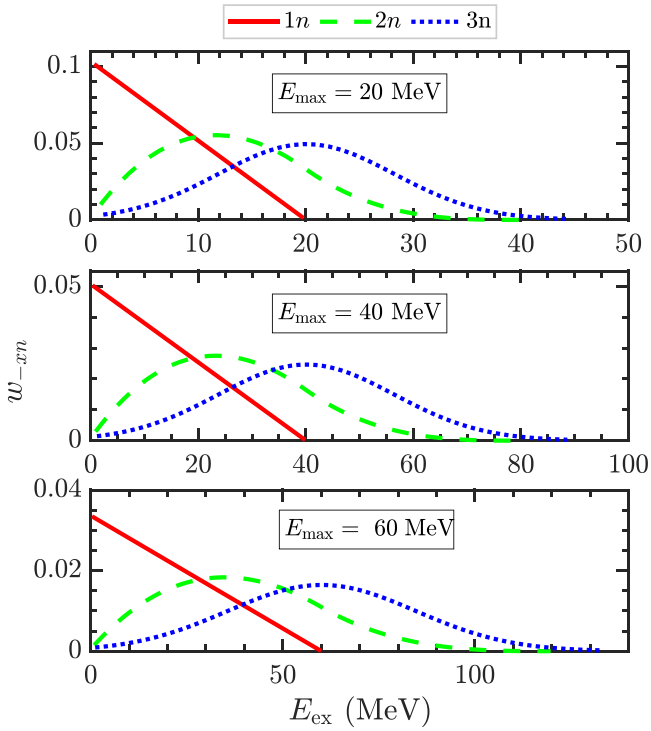

FIG. 3. Excitation energy distributions of the prefragment after the removal of $x = 1$–3 neutrons in direct fragmentation (abrasion stage), shown for $E_{max} = 20$, 40, and 60 MeV, respectively.

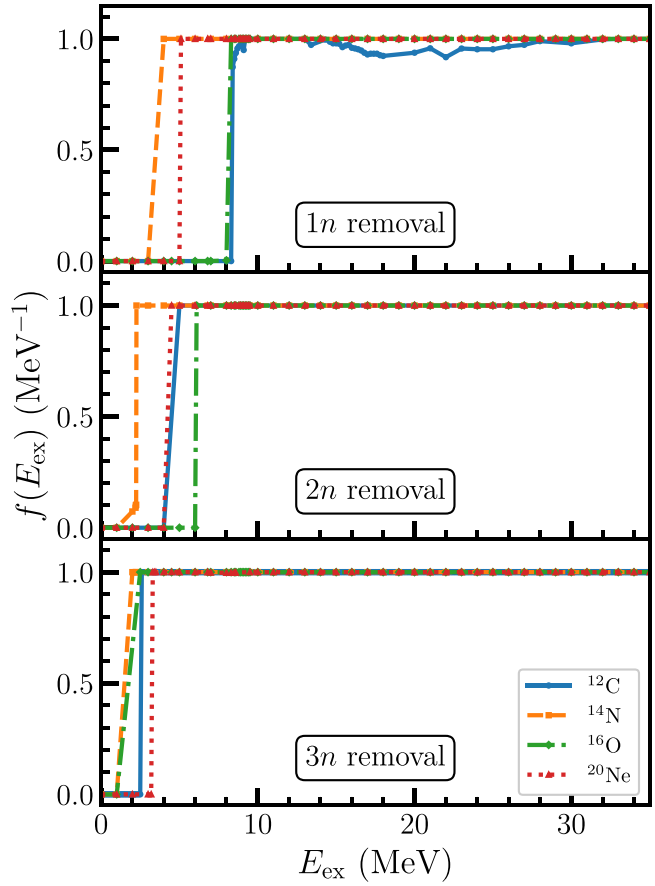

FIG. 4. Probability $[f(E_{ex}, A_P - x, Z_P)]$ of proton evaporation after initial removal of neutrons ($x = 1$–3) from the projectiles ^{12}C, ^{14}N, ^{16}O, and ^{20}Ne as a function of prefragment excitation energy (E_{ex}).

(GS) [42] model being one of the primary options. The prefragment excitation energy is determined by summing the energies of the hole states remaining in the core of the initial nucleus after nucleon removal. The GS model adopts a simple approach that uses a functional shape corresponds to an approximation of the single hole state density in the Woods-Saxon potential, as done in Refs. [33,34], requiring only two input parameters: the number of nucleons removed and the maximum excitation energy (E_{max}) of the prefragment formed following a one-nucleon removal reaction. E_{max} plays a crucial role in determining the excitation energy of prefragments in nuclear reactions. It represents the maximum energy that can be deposited by a single removed nucleon into the prefragment. Figure 3 illustrates the EED of the prefragment following the removal of one, two, and three nucleons from the nucleus. The distributions are characterized by the maximum excitation energy, which is set at 20, 40, and 60 MeV for the respective cases, for example. For one neutron abrasion case, the distribution is normalized and decreases linearly with increasing excitation energy until E_{max}, where it abruptly drops to zero. This behavior reflects the simplified assumption that the probability of excitation decreases as energy approaches the maximum limit. As more neutrons are removed, the EED generally becomes broader, more complex, and shifted towards higher energies. The mean energy [33] per removed nucleon $\langle E \rangle = (x/x+1)E_{max}$, which gives 10 MeV for the first neutron removal, for $E_{max} = 20$ MeV, and consequently this value increases and become maximum for higher neutron removal.

2. *Proton evaporation probability*

We now describe the calculation of the probability of proton evaporation $[f(E_{ex}, A_P - x, Z_P)]$ as a function of excitation energy. The calculations are performed using the LISE++ (GEMINI++) simulation code [15,43,44], which incorporates the Hauser-Feshbach and Weisskopf formalisms for compound nucleus decay. This approach accounts for decays involving the emission of at least one proton during cascade deexcitation. Figure 4 illustrates the variation in the charged-particle evaporation probability as a function of excitation energy (E_{ex}) for the prefragments of ^{12}C, ^{14}N, ^{16}O, and ^{20}Ne following the removal of one, two, and three neutrons during the abrasion stage. The evaporation probability curve begins to rise at or near the energy that equal to proton separation energy plus the Coulomb barrier for the prefragments. This is the excitation energy threshold beyond which the prefragment is sufficiently excited for charged-particle evaporation processes to occur. After this energy threshold, the prefragment nucleus loses at least one proton, which contributes to the charge-changing cross section. This trend is also followed by the other prefragments produced after the removal of two or three neutrons in the abrasion stage. With these values of $f(E_{ex})$ and $w_{-xn}(E_{ex})$, the evaporation probability (P_{-xn}) is calculated, and is shown in Fig. 5 for up to five neutron removals

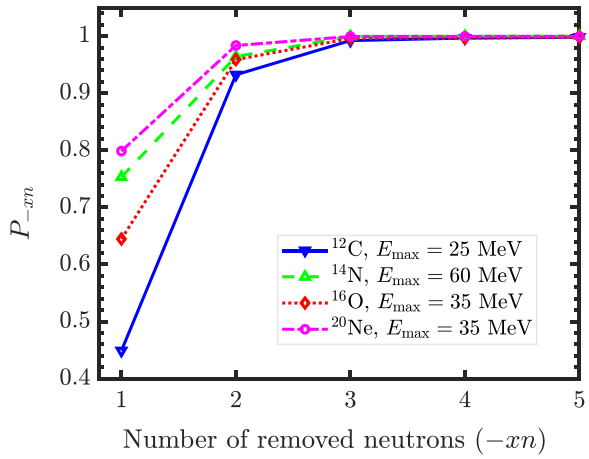

FIG. 5. Proton evaporation probability (P_{-xn}) as a function of the number of neutrons removed in the initial fragmentation (abrasion stage). The maximum excitation energy parameter E_{max} is selected to approximately reproduce the charge-changing cross-section data at 290 MeV/nucleon for a carbon target.

from the projectile. The parameter E_{max} is fixed to a value that reproduces the estimated evaporation cross sections from the experimental data at beam energy 290 MeV/nucleon on a carbon target. The variation of P_{-xn} indicates that, as the number of neutrons removed from the projectile increases, the charged-particle evaporation probability also increases. For all projectile nuclei, one notices this probability tends to 1 when the Z/N ratio becomes greater than 1, reflecting a direct relationship between the degree of neutron removal and the likelihood of charged-particle evaporation, contributing significantly to the charge-changing cross section.

Table II presents the contributions of proton evaporation (σ_{cc}^{evap}) [Eq. (11)] to the charge-changing cross section for various projectile nuclei (^{12}C, ^{14}N, ^{16}O, ^{20}Ne) on different elemental targets (C, Al, Cu) at a beam energy of 290 MeV/nucleon. The table is structured to show the neutron-removal cross sections (σ_{-xn}), which are calculated in the abrasion step using Eq. (4), for $1n$, $2n$, and $3n$ removal channels, along with their respective contributions to proton evaporation. The individual contributions from each neutron-removal channel to σ_{cc}^{evap} [Eq. (11)] are explicitly provided. The contributions $\sigma_{-xn,(x>3)}$ from neutron removal channels beyond $-3n$, such as the removal of four or more neutrons in the abrasion stage, are calculated and summed to estimate the contributions to the "$> -3n$" channel. The total evaporation contribution, σ_{cc}^{evap}, is then determined by summing the contributions from all neutron removal channels.

The last column of Table II is the evaporation estimate from experimental data [5,69], and is calculated by subtracting the charge-changing cross section (σ_{cc}) (Table I) using the Glauber model. The first column of the table represents the parameter E_{max}, which is varied to achieve an approximate match of σ_{cc}^{evap} with the estimated value extracted from the experimental data.

Figure 6 compares the ratio of evaporation contributions to charge-changing cross sections. The top panel (a) shows the ratio of the estimated evaporation contributions to the experimental charge-changing cross section, given by $(\sigma_{cc}^{expt} - \sigma_{cc})/\sigma_{cc}^{expt}$ on the left vertical axis, while the ratio $\sigma_{cc}^{evap}/\sigma_{cc}^{expt}$ is displayed on the right vertical axis. The bottom panel (b) represents the ratio of evaporation contributions in the abrasion stage, given by $\sigma_{cc}^{evap}/\sigma_{cc}$, which illustrates the influence of abrasion-stage calculations on the evaporation contributions. The plot compares these ratios for the projectiles ^{12}C, ^{14}N, ^{16}O, and ^{20}Ne interacting with three different elemental targets at a beam energy of approximately 290 MeV/nucleon.

The data in Table II demonstrate that reconciling theoretical proton evaporation contributions (σ_{cc}^{evap}) with the

TABLE II. Proton evaporation contributions (σ_{cc}^{evap}) [Eq. (11)] to charge-changing cross section for various projectile nuclei on elemental targets (C, Al, Cu) at a beam energy around 290 MeV/nucleon. The partial neutron removal cross sections (σ_{-xn}) [Eq. (4)] for $1n$, $2n$, $3n$, and beyond $3n$ channels are also shown, along with their respective contributions to σ_{cc}^{evap}. σ_{cc}^{evap} is calculated by summing up all the contributions from all neutron removal channels. For comparison, the evaporation contribution is also estimated by subtracting the Glauber charge-changing cross section [σ_{cc} (Table I)] from the experimental data (σ_{cc}^{expt}) taken from Refs. [5,69]. All cross sections in this table are rounded off to the nearest integer.

			σ_{-xn} (mb)				Contributions to σ_{cc}^{evap} (mb)					
E_{max} (MeV)	Nuclei	Target	σ_{-1n}	σ_{-2n}	σ_{-3n}	$\sigma_{-xn,(x>3)}$	$-1n$	$-2n$	$-3n$	$> -3n$	σ_{cc}^{evap} (mb)	$\sigma_{cc}^{expt} - \sigma_{cc}$ (mb)
25	^{12}C	C	114	28	8	1	50	26	8	1	85	81
15		Al	136	30	9	1	26	25	8	1	60	51
10		Cu	177	40	11	2	16	31	10	2	59	57
60	^{14}N	C	115	29	8	3	100	29	8	3	140	156
25		Al	137	34	10	4	88	33	9	4	134	120
15		Cu	165	42	12	4	92	41	11	4	148	146
35	^{16}O	C	115	29	9	3	69	27	9	3	108	106
20		Al	135	34	10	3	49	32	9	3	93	89
15		Cu	163	41	12	4	35	31	12	4	82	76
35	^{20}Ne	C	137	35	11	4	106	34	11	4	155	154
20		Al	159	40	12	6	92	36	12	6	146	137
10		Cu	186	47	14	7	48	36	14	7	105	94

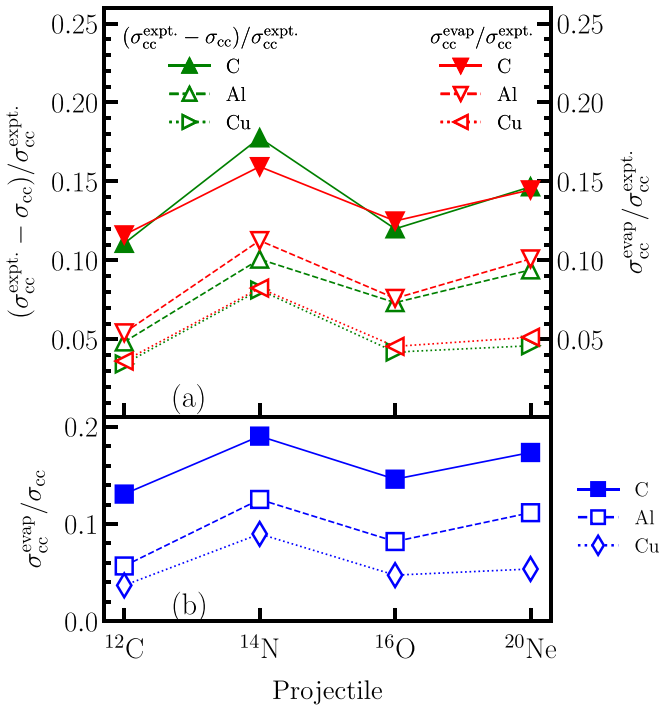

FIG. 6. The top panel (a) represents the ratio of the estimated evaporation contributions ($\sigma_{cc}^{expt.} - \sigma_{cc}$) to the total experimental charge-changing cross section ($\sigma_{cc}^{expt.}$) on the left vertical axis, while the ratio $\sigma_{cc}^{evap}/\sigma_{cc}^{expt.}$ is shown on the right vertical axis. The bottom panel (b) displays the ratio $\sigma_{cc}^{evap}/\sigma_{cc}$. Distinct marker styles differentiate the targets, with filled markers representing carbon and unfilled markers denoting aluminum and copper. Individual data points are marked, while lines serve as visual guides to indicate trends across different projectiles and targets.

estimation from experimental data ($\sigma_{cc}^{expt} - \sigma_{cc}$) requires lowering the parameter E_{max} (to ∼15MeV) for targets with a higher mass number and atomic number, e.g., Al, Cu, compared to lighter ones like C. This adjustment arises from target-dependent differences in initial neutron removal. Heavier targets induce 2–3 neutron removals during the projectile-target interaction in the abrasion stage, creating a neutron-deficient prefragment with an elevated proton-to-neutron ratio. Simultaneously, the neutron-deficient prefragment exhibits reduced binding energy, favoring competing decay pathways—particularly neutron reemission—which deplete excitation energy before protons can evaporate. Since neutron evaporation is not hindered by the Coulomb barrier, it becomes the dominant decay mode, effectively shifting the available excitation spectrum away from high-energy proton emission.

The parameter E_{max}, which defines the upper energy limit for proton emission in statistical decay models, must therefore be reduced for Al and Cu targets to reflect the redistribution of excitation energy and the increased dominance of neutron evaporation. Importantly, the target's role is limited to the initial neutron removal; subsequent evaporation occurs solely from the prefragment, independently of the target.

This suggests that proton evaporation becomes less significant as the mass of the target nucleus increases. In such cases, proton or charge particle removal from the projectile primarily occurs during the abrasion stage or direct fragmentation processes, where the nucleus breaks apart with less contribution from proton evaporation. The trend is more clearly illustrated in Fig. 6(b), which indicates that the ratio of evaporation contributions is greater with the carbon target in comparison to the other targets.

Figure 6 also reveals distinct trends among the projectiles, with ^{14}N consistently exhibiting the highest ratio for all target elements. The evaporation of neutrons and protons from the prefragment is governed by different underlying factors. Neutron emission is primarily determined by the neutron separation energy (S_n) and is favored in neutron-rich nuclei at low excitation energies ($E_{ex} \sim S_n$), where the absence of a Coulomb barrier allows evaporation even with limited energy. In contrast, proton evaporation requires overcoming both the proton separation energy (S_p) and the Coulomb barrier (V_c), making it viable only at high excitation energies ($E_{ex} \gg S_p + V_c$), particularly in proton-rich nuclei where excess protons enhance the likelihood of emission. When the initial abrasion stage preferentially removes neutrons from the projectile, the resulting prefragment becomes proton rich, further increasing the probability of proton evaporation. In such cases, the higher proton-to-neutron ratio makes proton emission more favorable compared to neutron emission, even at moderate excitation energies. In neutron rich nuclei, neutron evaporation remains dominant due to lower energy thresholds and higher nuclear level densities at low excitation energy. In neutron-deficient prefragments proton evaporation can become the preferred mode of deexcitation, often reaching near-unity probability as the Coulomb barrier effect diminishes. The analysis, as shown in Fig. 7 highlights the critical role of the separation energy difference, $\Delta S_{np} = S_{1n} - S_{1p}$, in governing charged-particle evaporation following neutron removal during abrasion for carbon target. Higher ΔS_{np} values, such as for ^{13}N ($\Delta S_{np} =$ 18.12 MeV), strongly favor proton emission due to the significantly higher energy required for additional neutron removal. Two neutron abrasion further amplifies ΔS_{np} in neutron-deficient prefragments, e.g., ^{14}O ($\Delta S_{np} = 18.56$ MeV), driven by symmetry energy and Coulomb effects [70]. These trends underscore ΔS_{np} as a key predictor of evaporation pathways in systems with fewer neutrons relative to protons.

The overall dominance of proton evaporation from the prefragment ^{13}N can be better understood by using a simplified representation of the ratio of proton to neutron decay width [71,72],

$$\frac{\Gamma_p}{\Gamma_n} \approx \frac{\exp[2\sqrt{a(E_{ex} - S_p - V_c - \delta_{eff})}]}{\exp[2\sqrt{a(E_{ex} - S_n - \delta_{eff})}]}, \tag{13}$$

with δ_{eff} as the pairing energy correction. The level density parameter is given by

$$a = \tilde{a}\left[1 + \frac{\Delta S}{U}[1 + \exp(-\gamma U)]\right], \tag{14}$$

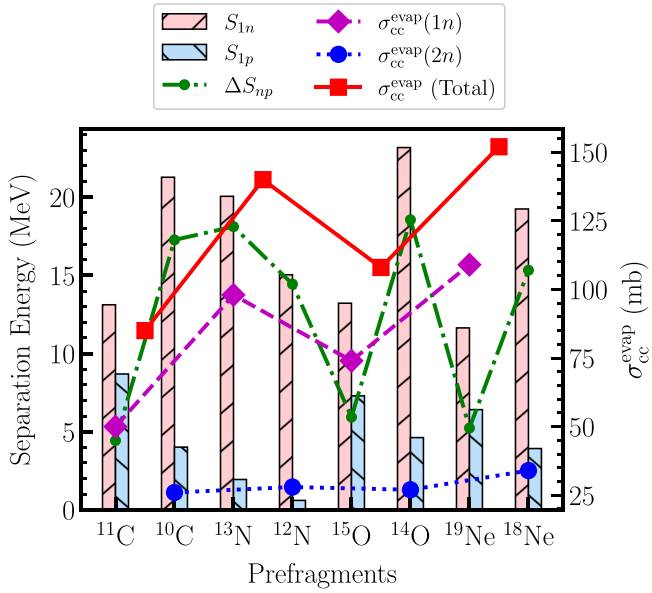

FIG. 7. Separation energies and evaporation cross sections for various prefragment nuclei. The neutron separation energy (S_{1n}) is represented by bars with forward-slash patterned shading, while the proton separation energy (S_{1p}) is depicted with backslash-patterned shading. The difference between neutron and proton separation energies (ΔS_{np}) is shown as a dashed-dotted line. Evaporation cross sections following one-neutron removal in the abrasion stage [$\sigma_{cc}^{evap}(1n)$] are represented by diamond markers with dashed lines, two-neutron removal [$\sigma_{cc}^{evap}(2n)$] by circular markers with dotted lines, and total evaporation cross sections [σ_{cc}^{evap}(Total)] by square markers with solid lines. The separation energy data are calculated using the atomic mass table from Ref. [74].

as suggested by Ignatyuk [73], where $\tilde{a}$ is the asymptotic level density parameter; this parameter is defined $\tilde{a} = 0.073A + 0.095A^{2/3}$. ΔS is the shell correction obtained from the difference between the experimental and the liquid drop model masses, U is the effective excitation energy, and γ is the shell damping factor. The ^{13}N prefragment, formed from ^{14}N after one-neutron removal in the abrasion stage, is characterized by a high level density, a low proton separation energy (S_p), a high neutron separation energy (S_n), and a low Coulomb barrier. These factors contribute to a significantly high decay width ratio (Γ_p/Γ_n), as illustrated in Fig. 8. This strongly favors proton evaporation, making it a dominant contributor to the charge-changing cross sections through proton emission. ^{11}C, the prefragment of ^{12}C after 1n removal in the abrasion stage, has the lowest decay width ratio (Γ_p/Γ_n) and consequently exhibits the smallest contribution to (σ_{cc}^{evap}) in Fig. 6, making it a limited contributor to charge-changing cross sections through proton emission.

The one-neutron separation energy (S_1) of the projectile further influences the residual excitation energy available for evaporation. High S_1 in neutron-deficient projectiles depletes excitation energy during neutron removal, reducing ablation, whereas low S_1 in neutron-rich systems preserves energy, enhancing ablation. Thus, projectiles with lower S_1 set a higher E_{max}, as evidenced by the linear E_{max}-S_1 correlation in Fig. 9, which holds across all targets.

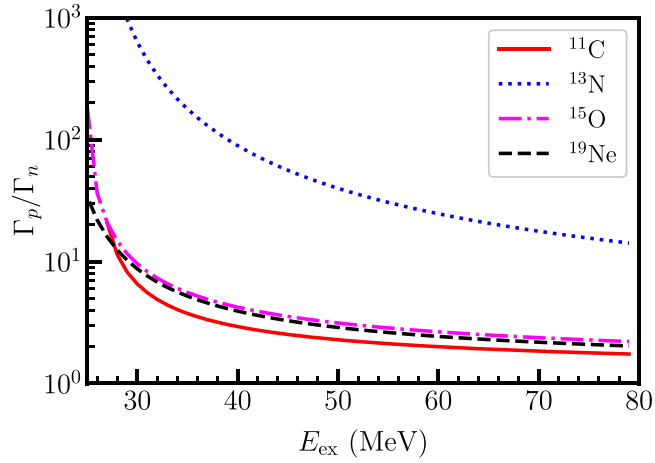

FIG. 8. Ratio of the proton to neutron decay widths as a function of the excitation energy of the prefragment after 1n removal from the projectiles.

These effects highlight the necessity of dynamically adjusting the maximum excitation energy parameter (E_{max}) in the evaporation model. Incorporating projectile specific properties—including neutron separation energy, neutron orbital occupancy, and beam energy—is crucial for accurately reproducing the observed dominance of abrasion (direct nucleon removal) in heavier target systems and ablation (evaporation) in lighter or neutron-rich projectiles.

Finally, let us address the possibility of constraining E_{max} microscopically or from systematics across more reactions. The excitation energy represents the energy imparted to the prefragment primarily due to the removal of nucleons. In the context of charge-changing reactions, this is dominated by neutron removal. EED describes the probability of different excitation energies following the interaction. The GS model

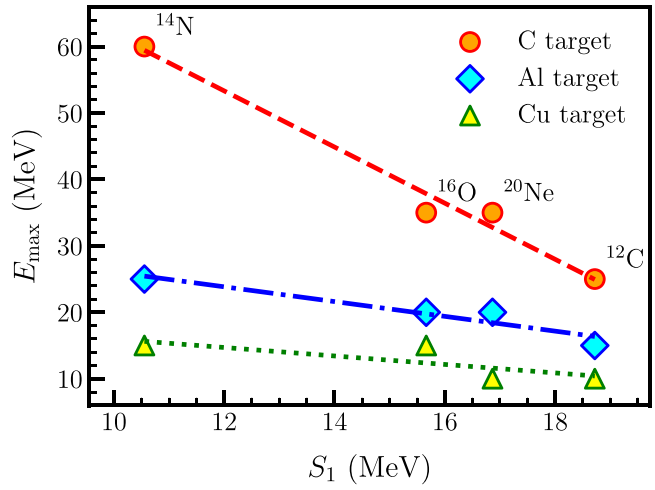

FIG. 9. Correlation between one neutron separation energy (S_1) from the projectile and the maximum excitation energy parameter (E_{max}) for different target materials (C, Al, Cu). The scatter points represent individual data for the projectiles ^{12}C, ^{14}N, ^{16}O, and ^{20}Ne, while the fitted lines illustrate the underlying trends for each target.

assumes that excitation arises mainly from the nuclear collision dynamics and reflects the statistical nature of the removal process, influenced by nuclear structure and the number of nucleons removed.

When not adjusted empirically, the parameter $E_{\max}$ is set equal to the Fermi energy at the center of the nucleus, $E_{\text{Fermi}}(0)$, thereby establishing a direct connection to intrinsic nuclear properties. The Fermi energy is calculated as [75]

$$E_{\text{Fermi}}(r) = \frac{\hbar^2}{2M}[3\pi^2\rho(r)]^{2/3},$$

where $\rho(r)$ is the neutron density and M is the nucleon mass. Since $\rho(0)$ generally increases with mass number and neutron excess, heavier or neutron-rich nuclei naturally exhibit higher central densities and hence larger $E_{\text{Fermi}}(0)$ and $E_{\max}$.

While in the present work $E_{\max}$ is tuned to experimental data for improved accuracy, this adjustment remains physically motivated. Moreover, we note that Refs. [69,76] provide a microscopic validation of this approach. In those studies, EEDs were calculated using the fully microscopic isospin-dependent quantum molecular dynamics (IQMD) model, which incorporates reaction dynamics without adjustable parameters. The comparisons presented in Ref. [69] for a few selected cases indicate that, although $E_{\max}$ is treated phenomenologically in the present model, the resulting values are consistent with independent microscopic predictions. This suggests that IQMD can serve as a reliable microscopic model to calibrate $E_{\max}$. By aligning the GS EED's shape (peak and width) with IQMD's for single-neutron removal, $E_{\max}$ can be constrained to physically motivated values. Extending IQMD simulations to lighter isotopes (e.g., C, N, O) could provide a more systematic $E_{\max}$ calibration across the studied systems. Nevertheless, future work aiming to constrain $E_{\max}$ systematically based on nuclear structure properties or fully microscopic reaction dynamics models would further enhance the predictive power and robustness of the approach.

IV. SUMMARY AND CONCLUSIONS

In this study, we calculated nuclear charge-changing cross sections for projectile nuclei, including ^{12}C, ^{14}N, ^{16}O, and ^{20}Ne, interacting with elemental targets such as carbon, aluminum, and copper at a beam energy of approximately 290 MeV/nucleon. We employed the abrasion-ablation model, which describes the fragmentation process in two stages: an initial abrasion phase, where nucleons are removed due to high-energy collisions, followed by an ablation phase, where the excited residual nucleus undergoes particle evaporation. Our calculations utilized the finite-range optical limit approximation within the Glauber model to describe the abrasion step of nuclear fragmentation, incorporating realistic nuclear density distributions. Additionally, we analyzed the ablation process by evaluating the evaporation contribution to charge-changing cross sections through a statistical decay model and by subtracting the abrasion component from the experimental data. We further examined how factors such as EED, particle decay widths, and separation energies influence charged-particle evaporation and its impact on charge-changing cross sections. Our findings indicate that, for heavier targets, the maximum excitation energy parameter ($E_{\max}$) tends to be lower when fitted to experimental data. Specifically, for a carbon target, we determined a higher $E_{\max}$ value around 35 ± 10 MeV, with the exception of ^{14}N, which exhibited an anomalous fitting around 60 MeV. In contrast, for aluminum and copper targets, the excitation energy parameter was consistently lower, around 15 ± 10 MeV. Furthermore, our analysis revealed an inverse linear correlation between $E_{\max}$ and the neutron separation energy of the projectile, highlighting the importance of projectile structure in determining the fragmentation process.

The ablation stage plays a crucial role in shaping the charge-changing cross-section measurements by influencing the final distribution of nuclear fragments. Our study underscores the necessity of precise modeling of the ablation process to improve the accuracy of theoretical predictions and experimental interpretations. In space, charge-changing cross sections are used to predict cosmic ray interactions with shielding and human tissues, aiding astronaut safety. In cancer therapy, they influence ion beam fragmentation, impacting dose delivery and treatment precision. Understanding these processes thus enhances space radiation protection, hadron therapy accuracy, and nuclear reactor safety. Moreover, our findings contribute to broader applications in astrophysics and cosmic ray propagation studies, where accurate modeling of nuclear fragmentation is essential.

Future work could explore refinements to the excitation energy parametrization by incorporating microscopic nuclear structure effects and extending calculations to a wider range of projectile-target combinations. Additionally, further experimental validation of the ablation model could help refine predictions, ultimately enhancing our understanding of nuclear fragmentation mechanisms.

ACKNOWLEDGMENTS

This work was supported by the Indo-Japan Cooperative Science Programme (IJCSP)-2023 under the DST-JSPS bilateral programs JPJSBP120247715, DST/INT/JSPS/P-393/2024(G), and in part supported by JSPS KAKENHI Grants No. 23K22485, No. 25K07285, and No. 25K01005. S.D. also acknowledges financial support from the Ministry of Education (MoE), India, through a doctoral fellowship.

DATA AVAILABILITY

The data supporting this study's findings are available within the article.

[1] J. W. Wilson, L. Townsend, H. Bidasaria, W. Schimmerling, M. Wong, and J. Howard, Neon-20 depth-dose relations in water, Health Phys. **46**, 1101 (1984).

[2] F. A. Cucinotta, M.-H. Y. Kim, and L. Ren, Evaluating shielding effectiveness for reducing space radiation cancer risks, Radiat. Meas. **41**, 1173 (2006).

[3] C. Zeitlin, A. Fukumura, S. Guetersloh, L. Heilbronn, Y. Iwata, J. Miller, and T. Murakami, Fragmentation cross sections of ^{28}Si at beam energies from 290 *A* to 1200 *A*MeV, Nucl. Phys. A **784**, 341 (2007).

[4] C. Zeitlin, S. Guetersloh, L. Heilbronn, J. Miller, A. Fukumura, Y. Iwata, T. Murakami, L. Sihver, and D. Mancusi, Fragmentation cross sections of medium-energy ^{35}Cl, ^{40}Ar, and ^{48}Ti beams on elemental targets, Phys. Rev. C **77**, 034605 (2008).

[5] C. Zeitlin, J. Miller, S. Guetersloh, L. Heilbronn, A. Fukumura, Y. Iwata, T. Murakami, S. Blattnig, R. Norman, and S. Mashnik, Fragmentation of ^{14}N, ^{16}O, ^{20}Ne, and ^{24}Mg nuclei at 290 to 1000 MeV/nucleon, Phys. Rev. C **83**, 034909 (2011).

[6] M. Notani, H. Sakurai, N. Aoi, H. Iwasaki, N. Fukuda, Z. Liu, K. Yoneda, H. Ogawa, T. Teranishi, T. Nakamura, H. Okuno, A. Yoshida, Y. X. Watanabe, S. Momota, N. Inabe, T. Kubo, S. Ito, A. Ozawa, T. Suzuki, I. Tanihata *et al.*, Projectile fragmentation reactions and production of nuclei near the neutron drip line, Phys. Rev. C **76**, 044605 (2007).

[7] G. Iancu, F. Flesch, and W. Heinrich, Nuclear fragmentation cross-sections of 400 A MeV ^{36}Ar and ^{40}Ar in collisions with light and heavy target nuclei, Radiat. Meas. **39**, 525 (2005).

[8] R. Silberberg, C. H. Tsao, and J. R. Letaw, Improvement of calculations of cross sections and cosmic-ray propagation, in *Composition and Origin of Cosmic Rays*, edited by M. M. Shapiro, NATO ASI Series Vol. 107 (Springer Netherlands, Dordrecht, 1983), p. 321.

[9] F. F. Badavi, L. W. Townsend, J. W. Wilson, and J. W. Norbury, An algorithm for a semiempirical nuclear fragmentation model, Comput. Phys. Commun. **47**, 281 (1987).

[10] J. W. Wilson, J. L. Shinn, L. W. Townsend, R. K. Tripathi, F. F. Badavi, and S. Y. Chun, NUCFRG2: A semiempirical nuclear fragmentation model, Nucl. Instrum. Methods Phys. Res. Sect. B **94**, 95 (1994).

[11] A. Adamczyk, R. Norman, S. Sriprisan, L. Townsend, J. Norbury, S. Blattnig, and T. Slaba, NUCFRG3: Light ion improvements to the nuclear fragmentation model, Nucl. Instrum. Methods Phys. Res. Sect. A **678**, 21 (2012).

[12] S. Agostinelli, J. Allison, K. Amako, J. Apostolakis, H. Araujo, P. Arce, M. Asai, D. Axen, S. Banerjee, G. Barrand, F. Behner, L. Bellagamba, J. Boudreau, L. Broglia, A. Brunengo, H. Burkhardt, S. Chauvie, J. Chuma, R. Chytracek, G. Cooperman *et al.*, GEANT4—a simulation toolkit, Nucl. Instrum. Methods Phys. Res. Sect. A **506**, 250 (2003).

[13] G. Battistoni, F. Cerutti, A. Fassò, A. Ferrari, S. Muraro, J. Ranft, S. Roesler, and P. R. Sala, The FLUKA code: Description and benchmarking, AIP Conf. Proc. **896**, 31 (2007).

[14] K. Niita, T. Sato, H. Iwase, H. Nose, H. Nakashima, and L. Sihver, PHITS—a particle and heavy ion transport code system, Radiat. Meas. **41**, 1080 (2006).

[15] O. Tarasov and D. Bazin, LISE++: Radioactive beam production with in-flight separators, Nucl. Instrum. Methods Phys. Res. B **266**, 4657 (2008).

[16] M. Krim, J. Inchaouh, N. Harakat, A. Khouaja, M. Fiak, M. R. Mesradi, A. Fathi, O. Jdair, and R. E. baydaoui, Cross sections, stopping power and Bragg peak range calculation of proton collisions with the DNA base adenine, Jpn. J. Appl. Phys. **58**, 096001 (2019).

[17] W. D. Newhauser and R. Zhang, The physics of proton therapy, Phys. Med. Biol. **60**, R155 (2015).

[18] A. Lühr, D. C. Hansen, R. Teiwes, N. Sobolevsky, O. Jäkel, and N. Bassler, The impact of modeling nuclear fragmentation on delivered dose and radiobiology in ion therapy, Phys. Med. Biol. **57**, 5169 (2012).

[19] F. Luoni, F. Horst, C. A. Reidel, A. Quarz, L. Bagnale, L. Sihver, U. Weber, R. B. Norman, W. de Wet, M. Giraudo, G. Santin, J. W. Norbury, and M. Durante, Total nuclear reaction cross-section database for radiation protection in space and heavy-ion therapy applications, New J. Phys. **23**, 101201 (2021).

[20] F. Horst, D. Schardt, H. Iwase, C. Schuy, M. Durante, and U. Weber, Physical characterization of ^{3}He ion beams for radiotherapy and comparison with ^{4}He, Phys. Med. Biol. **66**, 095009 (2021).

[21] O. Sokol, E. Scifoni, W. Tinganelli, W. Kraft-Weyrather, J. Wiedemann, A. Maier, D. Boscolo, T. Friedrich, S. Brons, M. Durante, and M. Krämer, Oxygen beams for therapy: Advanced biological treatment planning and experimental verification, Phys. Med. Biol. **62**, 7798 (2017).

[22] I. Tanihata, H. Savajols, and R. Kanungo, Recent experimental progress in nuclear halo structure studies, Prog. Part. Nucl. Phys. **68**, 215 (2013).

[23] R. Chatterjee and R. Shyam, Breakup reactions of light and medium mass neutron drip line nuclei, Prog. Part. Nucl. Phys. **103**, 67 (2018).

[24] A. Bonaccorso, Direct reaction theories for exotic nuclei: An introduction via semi-classical methods, Prog. Part. Nucl. Phys. **101**, 1 (2018).

[25] R. Chatterjee, Full quantal theory of one-neutron halo breakup reactions, Phys. Rev. C **68**, 044604 (2003).

[26] R. Chatterjee, P. Banerjee, and R. Shyam, Projectile structure effects in the Coulomb breakup of one-neutron halo nuclei, Nucl. Phys. A **675**, 477 (2000).

[27] V. Choudhary, W. Horiuchi, M. Kimura, and R. Chatterjee, Imprint of a nuclear bubble in nucleon-nucleus diffraction, Phys. Rev. C **102**, 034619 (2020).

[28] M. Grasso, L. Gaudefroy, E. Khan, T. Nikšić, J. Piekarewicz, O. Sorlin, N. Van Giai, and D. Vretenar, Nuclear "bubble" structure in ^{34}Si, Phys. Rev. C **79**, 034318 (2009).

[29] J. Barman, R. Barman, K. Parashar, and R. Chatterjee, The effect of exotic nuclear structure in determining the abundance of heavy elements in explosive nucleosynthesis, Eur. Phys. J.: Spec. Top. **233**, 2907 (2024).

[30] R. Chatterjee and M. Dan, Status of nuclear physics behind nucleosynthesis processes: The role of exotic neutron-rich nuclei, J. Astrophys. Astron. **41**, 51 (2020).

[31] J. Hüfner, K. Schäfer, and B. Schürmann, Abrasion-ablation in reactions between relativistic heavy ions, Phys. Rev. C **12**, 1888 (1975).

[32] B. V. Carlson, R. C. Mastroleo, and M. S. Hussein, Fragment production in heavy-ion reactions, Phys. Rev. C **46**, R30 (1992).

[33] C. Scheidenberger, I. A. Pshenichnov, K. Sümmerer, A. Ventura, J. P. Bondorf, A. S. Botvina, I. N. Mishustin, D. Boutin, S. Datz, H. Geissel, P. Grafström, H. Knudsen, H. F. Krause, B. Lommel, S. P. Møller, G. Münzenberg, R. H. Schuch, E. Uggerhøj, U. Uggerhøj, C. R. Vane *et al.*, Charge-changing interactions of ultrarelativistic Pb nuclei, Phys. Rev. C **70**, 014902 (2004).

[34] M. Tanaka, M. Takechi, A. Homma, A. Prochazka, M. Fukuda, D. Nishimura, T. Suzuki, T. Moriguchi, D. S. Ahn, A. Aimaganbetov, M. Amano, H. Arakawa, S. Bagchi, K.-H. Behr, N. Burtebayev, K. Chikaato, H. Du, T. Fujii, N. Fukuda, H. Geissel *et al.*, Charge-changing cross sections for $^{42-51}$Ca

and effect of charged-particle evaporation induced by neutron-removal reactions, Phys. Rev. C **106**, 014617 (2022).
[35] R. J. Glauber, High-energy collision theory, in *Lectures in Theoretical Physics*, edited by W. E. Brittin and L.G. Dunham (Interscience, New York, 1959), Vol. 1, p. 315.
[36] C. A. Bertulani and P. Danielewicz, *Introduction to Nuclear Reactions*, 2nd ed. (CRC, London, 2021).
[37] L. F. Oliveira, R. Donangelo, and J. O. Rasmussen, Abrasion-ablation calculations of large fragment yields from relativistic heavy ion reactions, Phys. Rev. C **19**, 826 (1979).
[38] E. Teixeira, T. Aumann, C. Bertulani, and B. Carlson, Nuclear fragmentation reactions as a probe of neutron skins in nuclei, Eur. Phys. J. A **58**, 205 (2022).
[39] S. Terashima, I. Tanihata, R. Kanungo, A. Estradé, W. Horiuchi, F. Ameil, J. Atkinson, Y. Ayyad, D. Cortina-Gil, I. Dillmann, A. Evdokimov, F. Farinon, H. Geissel, G. Guastalla, R. Janik, M. Kimura, R. Knoebel, J. Kurcewicz, Y. A. Litvinov, M. Marta *et al.*, Proton radius of ^{14}Be from measurement of charge-changing cross sections, Prog. Theor. Exp. Phys. **2014**, 101D02 (2014).
[40] Y. Suzuki, W. Horiuchi, S. Terashima, R. Kanungo, F. Ameil, J. Atkinson, Y. Ayyad, D. Cortina-Gil, I. Dillmann, A. Estradé, A. Evdokimov, F. Farinon, H. Geissel, G. Guastalla, R. Janik, R. Knoebel, J. Kurcewicz, Y. A. Litvinov, M. Marta, M. Mostazo *et al.*, Parameter-free calculation of charge-changing cross sections at high energy, Phys. Rev. C **94**, 011602(R) (2016).
[41] B. Abu-Ibrahim, W. Horiuchi, A. Kohama, and Y. Suzuki, Reaction cross sections of carbon isotopes incident on a proton, Phys. Rev. C **77**, 034607 (2008).
[42] J. J. Gaimard and K. H. Schmidt, A reexamination of the abrasion-ablation model for the description of the nuclear fragmentation reaction, Nucl. Phys. A **531**, 709 (1991).
[43] R. J. Charity, Systematic description of evaporation spectra for light and heavy compound nuclei, Phys. Rev. C **82**, 014610 (2010).
[44] D. Mancusi, R. J. Charity, and J. Cugnon, Unified description of fission in fusion and spallation reactions, Phys. Rev. C **82**, 044610 (2010).
[45] W. Horiuchi and N. Itagaki, Imprints of α clustering in the density profiles of ^{12}C, and ^{16}O, Phys. Rev. C **107**, L021304 (2023).
[46] Y. Yamaguchi, W. Horiuchi, and N. Itagaki, Evidence of bi-cluster structure in the ground state of ^{20}Ne, Phys. Rev. C **108**, 014322 (2023).
[47] W. Horiuchi and N. Itagaki, Density profiles near the nuclear surface of ^{44,52}Ti: An indication of α clustering, Phys. Rev. C **106**, 044330 (2022).
[48] T. Otsuka, T. Abe, T. Yoshida, Y. Tsunoda, N. Shimizu, N. Itagaki, Y. Utsuno, J. Vary, P. Maris, and H. Ueno, α-clustering in atomic nuclei from first principles with statistical learning and the Hoyle state character, Nat. Commun. **13**, 2234 (2022).
[49] M. Chernykh, H. Feldmeier, T. Neff, P. von Neumann-Cosel, and A. Richter, Structure of the Hoyle state in ^{12}C, Phys. Rev. Lett. **98**, 032501 (2007).
[50] See Supplemental Material at http://link.aps.org/supplemental/10.1103/PhysRevC.111.064604 for calculation of charge-changing cross sections with empirical densities.
[51] H. De Vries, C. De Jager, and C. De Vries, Nuclear charge-density-distribution parameters from elastic electron scattering, At. Data Nucl. Data Tables **36**, 495 (1987).
[52] L. C. Chamon, B. V. Carlson, L. R. Gasques, D. Pereira, C. De Conti, M. A. G. Alvarez, M. S. Hussein, M. A. Cândido Ribeiro, E. S. Rossi, and C. P. Silva, Toward a global description of the nucleus-nucleus interaction, Phys. Rev. C **66**, 014610 (2002).
[53] J. L. Friar, J. Martorell, and D. W. L. Sprung, Nuclear sizes and the isotope shift, Phys. Rev. A **56**, 4579 (1997).
[54] T. Yamaguchi, I. Hachiuma, A. Kitagawa, K. Namihira, S. Sato, T. Suzuki, I. Tanihata, and M. Fukuda, Scaling of charge-changing interaction cross sections and point-proton radii of neutron-rich carbon isotopes, Phys. Rev. Lett. **107**, 032502 (2011).
[55] I. Abdul-Magead and B. Abu-Ibrahim, Contribution of the projectile neutrons to the total charge-changing cross sections, Nucl. Phys. A **1000**, 121804 (2020).
[56] G. Fan and X. Zhan, Influence of neutrons on charge-changing cross-sections, Int. J. Mod. Phys. E **28**, 1950070 (2019).
[57] T. Yamaguchi, M. Fukuda, S. Fukuda, G. W. Fan, I. Hachiuma, M. Kanazawa, A. Kitagawa, T. Kuboki, M. Lantz, M. Mihara, M. Nagashima, K. Namihira, D. Nishimura, Y. Okuma, T. Ohtsubo, S. Sato, T. Suzuki, M. Takechi, and W. Xu, Energy-dependent charge-changing cross sections and proton distribution of ^{28}Si, Phys. Rev. C **82**, 014609 (2010).
[58] A. Bhagwat and Y. K. Gambhir, Microscopic investigations of mass and charge changing cross sections, Phys. Rev. C **69**, 014315 (2004).
[59] B. Alpat, E. Pilicer, S. Blasko, D. Caraffini, F. D. Capua, V. Postolache, G. Saltanocchi, M. Menichelli, L. Desorgher, M. Durante, R. Pleskac, and C. L. Tessa, IEEE Trans. Nucl. Sci. **60**, 4673 (2013).
[60] D. T. Tran, H. J. Ong, T. T. Nguyen, I. Tanihata, N. Aoi, Y. Ayyad, P. Y. Chan, M. Fukuda, T. Hashimoto, T. H. Hoang, E. Ideguchi, A. Inoue, T. Kawabata, L. H. Khiem, W. P. Lin, K. Matsuta, M. Mihara, S. Momota, D. Nagae, N. D. Nguyen *et al.*, Charge-changing cross-section measurements of $^{12-16}$C at around 45*A* MeV and development of a glauber model for incident energies 10*A*–2100*A* MeV, Phys. Rev. C **94**, 064604 (2016).
[61] I. Schall, D. Schardt, H. Geissel, H. Irnich, E. Kankeleit, G. Kraft, A. Magel, M. Mohar, G. Münzenberg, F. Nickel, C. Scheidenberger, and W. Schwab, Charge-changing nuclear reactions of relativistic light-ion beams ($5 \leqslant Z \leqslant 10$) passing through thick absorbers, Nucl. Instrum. Methods Phys. Res. B **117**, 221 (1996).
[62] P. Ferrando, W. R. Webber, P. Goret, J. C. Kish, D. A. Schrier, A. Soutoul, and O. Testard, Measurement of ^{12}C, ^{16}O, and ^{56}Fe charge changing cross sections in helium at high energy, comparison with cross sections in hydrogen, and application to cosmic-ray propagation, Phys. Rev. C **37**, 1490 (1988).
[63] L. Chulkov, O. Bochkarev, D. Cortina-Gil, H. Geissel, M. Hellström, M. Ivanov, R. Janik, K. Kimura, T. Kobayashi, A. Korsheninnikov, G. Münzenberg, F. Nickel, A. Ogloblin, A. Ozawa, M. Pfützner, V. Pribora, M. Rozhkov, H. Simon, B. Sitár, P. Strmen *et al.*, Total charge-changing cross sections for neutron-rich light nuclei, Nucl. Phys. A **674**, 330 (2000).
[64] A. N. Golovchenko, J. Skvarč, N. Yasuda, M. Giacomelli, S. P. Tretyakova, R. Ilić, R. Bimbot, M. Toulemonde, and T. Murakami, Total charge-changing and partial cross-section measurements in the reactions of ∼110–250 MeV/nucleon ^{12}C in carbon, paraffin, and water, Phys. Rev. C **66**, 014609 (2002).
[65] S. Cecchini, T. Chiarusi, G. Giacomelli, M. Giorgini, A. Kumar, G. Mandrioli, S. Manzoor, A. Margiotta, E. Medinaceli, L.

Patrizii, V. Popa, I. Qureshi, G. Sirri, M. Spurio, and V. Togo, Fragmentation cross sections of Fe^{26+}, Si^{14+} and C^{6+} ions of 0.3–10 A GeV on polyethylene, CR39 and aluminum targets, Nucl. Phys. A **807**, 206 (2008).

[66] W. R. Webber, J. C. Kish, and D. A. Schrier, Total charge and mass changing cross sections of relativistic nuclei in hydrogen, helium, and carbon targets, Phys. Rev. C **41**, 520 (1990).

[67] J.-X. Cheng, D.-H. Zhang, S.-W. Yan, J.-S. Li, L.-C. Wang, Y.-J. Li, and N. Yasuda, The fragmentation of ^{20}Ne at 400 A MeV, Chin. Phys. C **36**, 37 (2012).

[68] D.-H. Zhang, J.-X. Cheng, S. Kodaira, and N. Yasuda, Projectile fragmentation of 388 A MeV ^{20}Ne in polyethylene, carbon and aluminum targets, Nucl. Instrum. Methods Phys. Res. B **286**, 238 (2012).

[69] J. Zhao, B.-H. Sun, I. Tanihata, S. Terashima, A. Prochazka, J. Xu, L. Zhu, J. Meng, J. Su, K. Zhang, L. Geng, L. He, C. Liu, G. Li, C. Lu, W. Lin, W. Lin, Z. Liu, P. Ren, Z. Sun *et al.*, Isospin-dependence of the charge-changing cross-section shaped by the charged-particle evaporation process, Phys. Lett. B **847**, 138269 (2023).

[70] S. Burrello, M. Colonna, and H. Zheng, The symmetry energy of the nuclear EoS: a study of collective motion and low-energy reaction dynamics in semiclassical approaches, Front. Phys. **7**, 53 (2019).

[71] J. Benlliure, P. Armbruster, M. Bernas, C. Böckstiegel, S. Czajkowski, C. Donzaud, H. Geissel, A. Heinz, C. Kozhuharov, P. Dessagne, G. Münzenberg, M. Pfützner, W. Schwab, L. Tassan-Got, and B. Voss, Production of medium-weight isotopes by fragmentation in 750 A MeV ^{238}U on ^{208}Pb collisions, Eur. Phys. J. A **2**, 193 (1998).

[72] W. C. de Wet, L. W. Townsend, W. P. Ford, C. M. Werneth, R. B. Norman, and T. C. Slaba, Improvements to a quantum mechanical abrasion-ablation model of nuclear fragmentation: Revised nuclear level densities and improved ablation code, Nucl. Instrum. Methods Phys. Res. B **480**, 115 (2020).

[73] A. V. Ignatyuk, G. N. Smirenkin, and A. S. Tishin, Phenomenological description of energy dependence of the level density parameter, Yad. Fiz. **21**, 485 (1975) [Sov. J. Nucl. Phys. **21**, 255 (1975)].

[74] M. Wang, W. J. Huang, F. G. Kondev, G. Audi, and S. Naimi, The AME 2020 atomic mass evaluation (II). Tables, graphs and references, Chin. Phys. C **45**, 030003 (2021).

[75] A. Prochazka and M. Takechi, Nurex physics manual, https://www.isotopea.com/nurex/nurex.pdf.

[76] J. Su, F.-S. Zhang, and B.-A. Bian, Odd-even effect in heavy-ion collisions at intermediate energies, Phys. Rev. C **83**, 014608 (2011).